Ultrafast population dynamics in electrically modulated terahertz quantum cascade lasers

New Journal of Physics
The open access journal for physics

Ultrafast population dynamics in electrically modulated terahertz quantum cascade lasers

F Wang, X G Guo, C Wang and J C Cao[1]

Key Laboratory of Terahertz Solid-State Technology, Shanghai Institute of Microsystem and Information Technology, Chinese Academy of Sciences, 865 Changning Road, Shanghai 200050, People's Republic of China
E-mail: jccao@mail.sim.ac.cn

New Journal of Physics **15** (2013) 075009 (12pp)
Received 18 April 2013
Published 16 July 2013
Online at http://www.njp.org/
doi:10.1088/1367-2630/15/7/075009

Abstract. The ultrafast population dynamics in electrically modulated three-well terahertz quantum cascade lasers (QCLs) is studied by using the self-consistent Bloch–Poisson equations. In the modulation process, the non-equilibrium oscillations of the population inversion are found before the population equilibrium recovers. The equilibrium formation time increases nonlinearly with the period number. This phenomenon stems from the non-uniform distribution of the electric potential. In different periods, different responses to the electrical modulation are also explored. An in-depth understanding of electron transport in the cascade structure is obtained. Finally, we demonstrate the feasibility of a modulation frequency up to gigahertz in terahertz QCLs.

[1] Author to whom any correspondence should be addressed.

Contents

1. Introduction

Terahertz quantum cascade lasers (QCLs) are electrically pumped coherent radiation sources in the terahertz region [1]. As compact and powerful semiconductor lasers, terahertz QCLs have been widely studied [2]. However, owing to the complexity of the cascade structure, the electron transport of the terahertz QCL cannot be perfectly simulated. Currently, Monte Carlo (MC) and density matrix approaches are two important theoretical simulation methods that are normally used to analyze the electron transport in terahertz QCLs and these two methods are still in development [3–7]. Most simulations adopt the cyclic boundary approximation and the emitter injection was not considered. So, the electron system in these simulations is closed. In our previous work, the terahertz QCL has been treated as an open system in which the emitter injection was taken into account [8]. The non-uniform distribution and the dynamic equilibrium of the electric potential in active regions were found. These phenomena were explained by the microscopic self-adaptive process of the biased cascade structure [8].

The dc modulation of terahertz QCLs has been realized up to tens of gigahertz by using the radio frequency (RF) synthesizer and bias-T [9, 10]. Although the RF modulation has already been used to realize the mid-infrared wireless communication by utilizing mid-infrared QCLs [11], the analogous technique is not used in terahertz wireless transmission until now. Direct amplitude modulation (AM) approaches, such as on–off keying (OOK), are adopted for wireless communication in terahertz region by using terahertz QCLs. And the time domain signal can be detected by a terahertz quantum well photodetector (QWP). The direct modulation rate of several megahertz has been realized and perfect modulation signals in the time domain can be obtained [12]. On the other hand, the coherent asynchronous sampling of the actively mode-locked terahertz QCL has been shown [13]. Recently, direct intensity sampling in the time domain of the mode-locked terahertz QCL was provided by the technique similar to the terahertz time domain spectroscopy [14]. According to the above researches, terahertz QCLs are verified as potential sources for high-speed data transmission in the terahertz band. In these cases, the fast modulation has been adopted. In the modulation, the population equilibrium recovery process is not only a key element for realizing the fast modulation but also for providing a lot of information about physical mechanisms of the electron transport in terahertz QCLs.

The electron transport in terahertz QCLs is mainly based on the intersubband transitions in the conduction band. The intersubband scattering processes are very fast, especially the longitudinal optical phonon–electron scattering in resonant-phonon-designed terahertz QCLs.

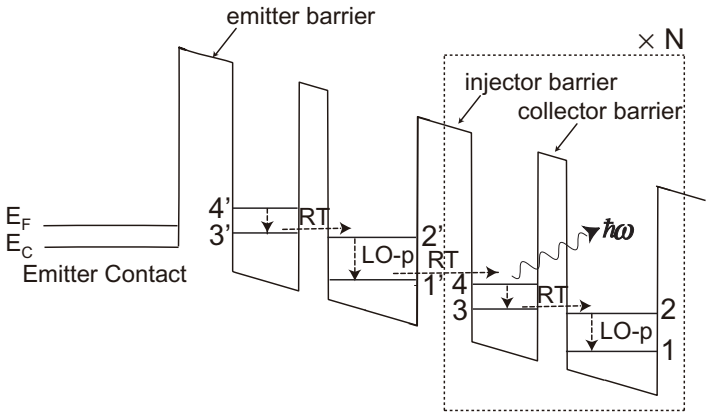

Figure 1. The schematic band diagram of the active region and emitter contact. There are two modules and four subbands in one period. Injector barrier and collector barrier between modules are also indicated.

So in a view of the cyclic boundary approximation, it can be easily understood that the fast relaxation leads to the fast equilibrium recovery process. But in the real situation, the cascade structure has several hundreds of quantum wells, and electrons should travel a long distance from the emitter contact layer to the last period. After the electrical modulation is applied, besides the direct change of the electric potential, electron accumulation and depletion in the device are varied and then the distribution of the electric potential is affected. So, the equilibrium recovery process seems to be very complicated.

In order to investigate the electron transport in the cascade structure, we introduce self-consistent Bloch–Poisson equations to simulate the modulation process. We find non-equilibrium oscillations of the population inversion after the applied electric field changes. Different equilibrium formation times with different period numbers are also found. The electron transport is affected by the non-uniform distribution of the electric potential. At last, we discuss the population dynamics with the modulation frequency up to gigahertz.

2. Open system simulation for terahertz quantum cascade lasers

2.1. Terahertz quantum cascade laser model

In this work, we focus on a terahertz QCL based on the resonant phonon three-well active region. It was first realized by Luo *et al* [15] and was then studied extensively [6–8, 16]. The highest terahertz QCL-operating temperature of 199.5 K has been achieved by the three-well phonon-assisted active region [17].

The schematic band diagram of the emitter contact and active region is presented in figure 1. We separate one period into two modules, which are as similar as [6]: one is the active double well and the other one is the phonon well. The center 36 Å of the 161 Å phonon well is doped with Si to $10^{17}\,\mathrm{cm}^{-3}$, similar to [12]. Electrons are first injected into the bound state $4'$ from three-dimensional states of the emitter contact. Electron transport in the terahertz QCL-active regions follows the scattering and resonant tunneling mechanisms. Simple resonant tunnelings through injector and collector barriers between the above mentioned two modules are considered. The Hamiltonian of the four-level system including the resonant tunneling

interaction is given by

$$H = \begin{pmatrix} E_{1'} & -\frac{\Delta_{1'4}}{2} & -\frac{\Delta_{1'3}}{2} & 0 \\ -\frac{\Delta_{1'4}}{2} & E_4 & 0 & -\frac{\Delta_{42}}{2} \\ -\frac{\Delta_{1'3}}{2} & 0 & E_3 & -\frac{\Delta_{32}}{2} \\ 0 & -\frac{\Delta_{42}}{2} & -\frac{\Delta_{32}}{2} & E_2 \end{pmatrix}, \tag{1}$$

where Δ_{ab} is the anticrossing gap of subbands a and b. The other resonant tunneling channels are not included, because they are not important in the operating applied electric field around the optimal site 14.0 kV cm^{-1}.

2.2. Emitter injection

In some two-dimensional quantum devices, such as QWP, the thermionic field-assisted tunneling and thermionic emission are the two most important injection mechanisms because of the wide quantum barrier adjacent to the contact [18]. However, the emitter barrier width in terahertz QCLs is much narrower (e.g. 4.8 nm for this present laser) and the operating temperature is 25 K in this work. So, the above two injection mechanisms are not important here.

Similar to resonant tunneling diodes (RTD), we believe that the most important physical mechanism of the emitter injection is resonant tunneling in terahertz QCLs. The injection current density from the emitter contact can be expressed as [18]

$$J_{\text{inj}} = \frac{em_e k_B T}{2\pi^2 \hbar^3} \int_{E_{\text{em}}}^{\infty} T_c \ln\left[1 + \exp\left(\frac{E_{\text{F,em}} - E}{k_B T}\right)\right] dE, \tag{2}$$

where E_{em} and $E_{\text{F,em}}$ are the conduction band edge and the Fermi level of the emitter contact, respectively. As for the contact doping of 5×10^{18} cm^{-3}, the calculated $E_{\text{F,em}}$ is 2.88 meV above the conduction band bottom. Here, we neglect the inverse current density from the quantum well to the emitter contact which is not significant with such a high applied electric field. e is the magnitude of the electronic charge, T is the working temperature and T_c is the tunneling coefficient. T_c can be described as [19, 20]

$$T_c = \frac{\Gamma^2/4}{\Gamma^2/4 + (E - E_3)^2}, \tag{3}$$

where Γ is the full-width at half-maximum of the resonance associated with E_3. E_3 is the energy of subband 3 in the adjacent active double well of the emitter contact, and it is considered as the resonance energy. Γ is inversely proportional to the lifetime of subband 3 and can be approximately described as $\hbar/\tau_3$ [20]. Since Γ and E_3 change with the electric field, T_c is finally a function of electric field. Here, we only consider subband 3 as the resonance subband, because the energy of subband 4 is much higher than the Fermi level of the emitter contact. Subband 2 is localized in the phonon well with the applied electric field range in this work.

2.3. Multi-period self-consistent Bloch–Poisson equations

We briefly introduce the equations here. First, we simulate the terahertz QCL by using the MC method, and then set up a look-up table including the required physical quantities under different electric fields. In the study of the steady state, the distribution of the electric potential slightly deviates from the applied electric field [8]. So, the physical quantities obtained by MC simulations are self-consistently confirmed to be available to use. If the electric potential shows strong non-uniformity, the look-up table cannot be used.

Then, we solve multi-period four-level Bloch equations which can be written as

$$\begin{aligned}
\frac{\mathrm{d}}{\mathrm{d}t}P_{1'4,n} &= -\frac{\mathrm{i}}{\hbar}\varepsilon_{1'4,n}P_{1'4,n} + \frac{\mathrm{i}\Delta_{1'4}}{2\hbar}(N_{1,n-1} - N_{4,n}) + \frac{\mathrm{d}}{\mathrm{d}t}\,P_{1'4,n}\big|_{\mathrm{dep}}\,,\\
\frac{\mathrm{d}}{\mathrm{d}t}P_{1'3,n} &= -\frac{\mathrm{i}}{\hbar}\varepsilon_{1'3,n}P_{1'3,n} + \frac{\mathrm{i}\Delta_{1'3}}{2\hbar}(N_{1,n-1} - N_{3,n}) + \frac{\mathrm{d}}{\mathrm{d}t}\,P_{1'3,n}\big|_{\mathrm{dep}}\,,\\
\frac{\mathrm{d}}{\mathrm{d}t}P_{42,n} &= -\frac{\mathrm{i}}{\hbar}\varepsilon_{42,n}P_{42,n} + \frac{\mathrm{i}\Delta_{42}}{2\hbar}(N_{4,n} - N_{2,n}) + \frac{\mathrm{d}}{\mathrm{d}t}\,P_{42,n}\big|_{\mathrm{dep}}\,,\\
\frac{\mathrm{d}}{\mathrm{d}t}P_{32,n} &= -\frac{\mathrm{i}}{\hbar}\varepsilon_{32,n}P_{32,n} + \frac{\mathrm{i}\Delta_{32}}{2\hbar}(N_{3,n} - N_{2,n}) + \frac{\mathrm{d}}{\mathrm{d}t}\,P_{32,n}\big|_{\mathrm{dep}}\,,\\
\frac{\mathrm{d}}{\mathrm{d}t}N_{4,n} &= \frac{\Delta_{1'4}}{\hbar}\mathrm{Im}\,P_{1'4,n} - \frac{\Delta_{42}}{\hbar}\mathrm{Im}\,P_{42,n} + \frac{\mathrm{d}}{\mathrm{d}t}\,N_{4,n}\big|_{\mathrm{scatt}}\,,\\
\frac{\mathrm{d}}{\mathrm{d}t}N_{3,n} &= \frac{\Delta_{1'3}}{\hbar}\mathrm{Im}\,P_{1'3,n} - \frac{\Delta_{32}}{\hbar}\mathrm{Im}\,P_{32,n} + \frac{\mathrm{d}}{\mathrm{d}t}\,N_{3,n}\big|_{\mathrm{scatt}}\,,\\
\frac{\mathrm{d}}{\mathrm{d}t}N_{2,n} &= \frac{\Delta_{32}}{\hbar}\mathrm{Im}\,P_{32,n} + \frac{\Delta_{42}}{\hbar}\mathrm{Im}\,P_{42,n} + \frac{\mathrm{d}}{\mathrm{d}t}\,N_{2,n}\big|_{\mathrm{scatt}}\,,\\
\frac{\mathrm{d}}{\mathrm{d}t}N_{1,n} &= -\frac{\Delta_{1'4}}{2\hbar}\mathrm{Im}\,P_{1'4,n+1} - \frac{\Delta_{1'3}}{2\hbar}\mathrm{Im}\,P_{1'3,n+1} + \frac{\mathrm{d}}{\mathrm{d}t}\,N_{1,n}\big|_{\mathrm{scatt}}\,.
\end{aligned} \tag{4}$$

Here, $N_{a,n}$ is the electron sheet density of subband a and $P_{ab,n}$ is the polarization between subbands a and b in the period n. $\varepsilon_{ab,n}$ is the energy difference between subbands a and b, in which the subband $1'$ is in the period $n-1$. The last items in polarization differential functions are the dephasing items, which have been introduced clearly in [3]. The dephasing item can be written as

$$\frac{\mathrm{d}}{\mathrm{d}t}\,P_{ab,n}\big|_{\mathrm{dep}} = P_{ab,n}\left(\frac{1}{2\tau_{a,n}} + \frac{1}{2\tau_{b,n}} + \frac{1}{\tau_{\mathrm{pure}}}\right). \tag{5}$$

Here, $\tau_{a,n}$ is the lifetime of subband a for period n and τ_{pure} is the pure dephasing time. In this work, the pure dephasing time 0.75 ps and the emitter contact doping density $5\times10^{18}\,\mathrm{cm}^{-3}$ are the same with [8]. The last items in electron sheet density differential functions are the intersubband scatterings. The electron injection should be added to the differential function in the first period. And the electron depletion of the phonon well should also be added in the last period.

The electron distribution is changed after solving the Bloch equations. Then, the built-in electric potential is obtained by solving the Poisson's equation which can be described as

$$\frac{\mathrm{d}^2\varphi}{\mathrm{d}z^2} = -\frac{|e|}{\varepsilon}[N_{\mathrm{D}} - n], \tag{6}$$

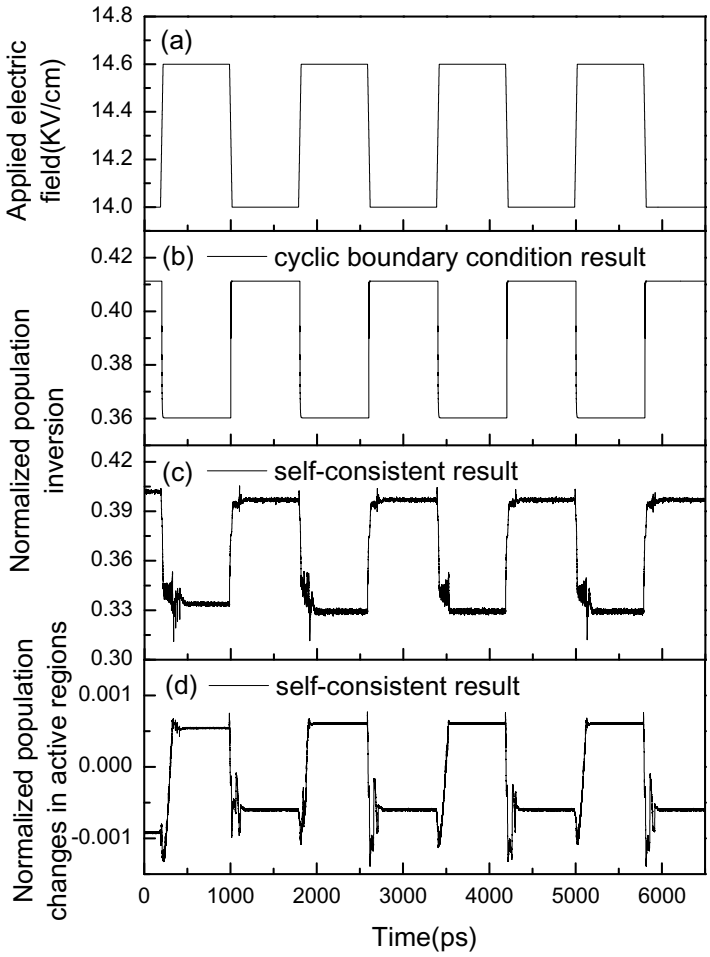

Figure 2. (a) The modulated applied electric field. The calculated modulated normalized population inversion between subbands 4 and 3 with the cyclic boundary approximation (b) and the multi-period self-consistent method (c) in time domain. (d) The calculated normalized population changes in active regions with the self-consistent method. The period number is set at 100 when the self-consistent method is adopted in (c) and (d).

where N_D is the active region doping concentration and n is the electron distribution. The changed electric potential, in turn, affects the electron distribution. The distribution of electrons and the electric potential will achieve equilibrium eventually, after calculating of the multi-period self-consistent Bloch–Poisson equations.

3. Electrical modulation results

In this section, we give simulation results of population dynamics in the electrically modulated terahertz QCL. We mainly consider the population inversion between lasing subbands 4 and 3 as the most concerned parameter. In the self-consistent simulation, the population inversion is averaged by the period number. And in order to understand the population dynamics clearly, we also give normalized population changes in active regions. The normalized population change

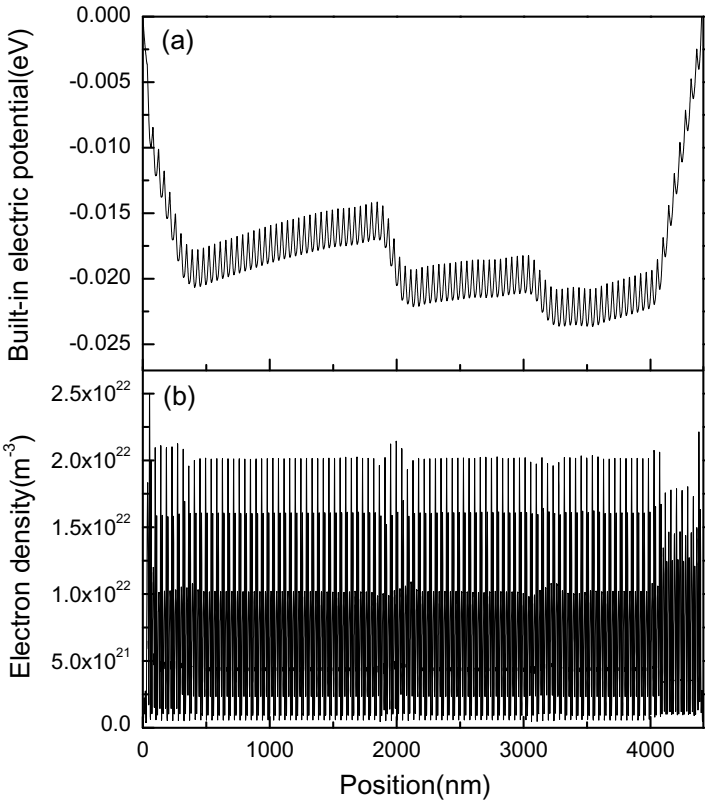

Figure 3. The built-in electric potential (a) and the electron density (b) corresponding to the position. The period number is 100.

can be described as $(N_{\mathrm{inj}} - N_{\mathrm{dep}})/N_{\mathrm{tot}}$, where N_{inj}, N_{dep} and N_{tot} are the injected electron number from the emitter contact, the depleted electron number of the last period and the total electron number in active regions, respectively.

First, we simulate the electrical modulation process in cyclic boundary condition and then compare it with the self-consistent result. In figure 2(a), we give the square wave as the modulated signal with the electric field amplitude 0.6 kV cm^{-1}, the falling (rising) time 30 ps, the duty cycle 0.5 and the pulse width 800 ps. In fact, the OOK modulation without RF synthesizer is hard to be realized over gigahertz. On the other hand, such a long pulse width can ensure the establishment of the population equilibrium. The population inversions change when the applied electric field is modulated.

The population inversions with different boundary conditions are shown in figures 2(b) and (c). It can be found that the result with the cyclic boundary approximation appears to be smooth and the self-consistent result is totally different. First of all, in figure 2(c), non-equilibrium oscillations of the population inversion have been found before the population equilibrium recovers, after both the falling edge and the rising edge. The equilibrium formation times are apparently larger than the falling (rising) time. It is very different with the situation of the cyclic boundary approximation that the population equilibrium is established as quickly as the changing applied electric field. This phenomenon will be explained by more calculated results in the following. In addition, when the self-consistent method is adopted, the equilibrium state of the normalized population inversion is not stabilized at a fixed value. It can be

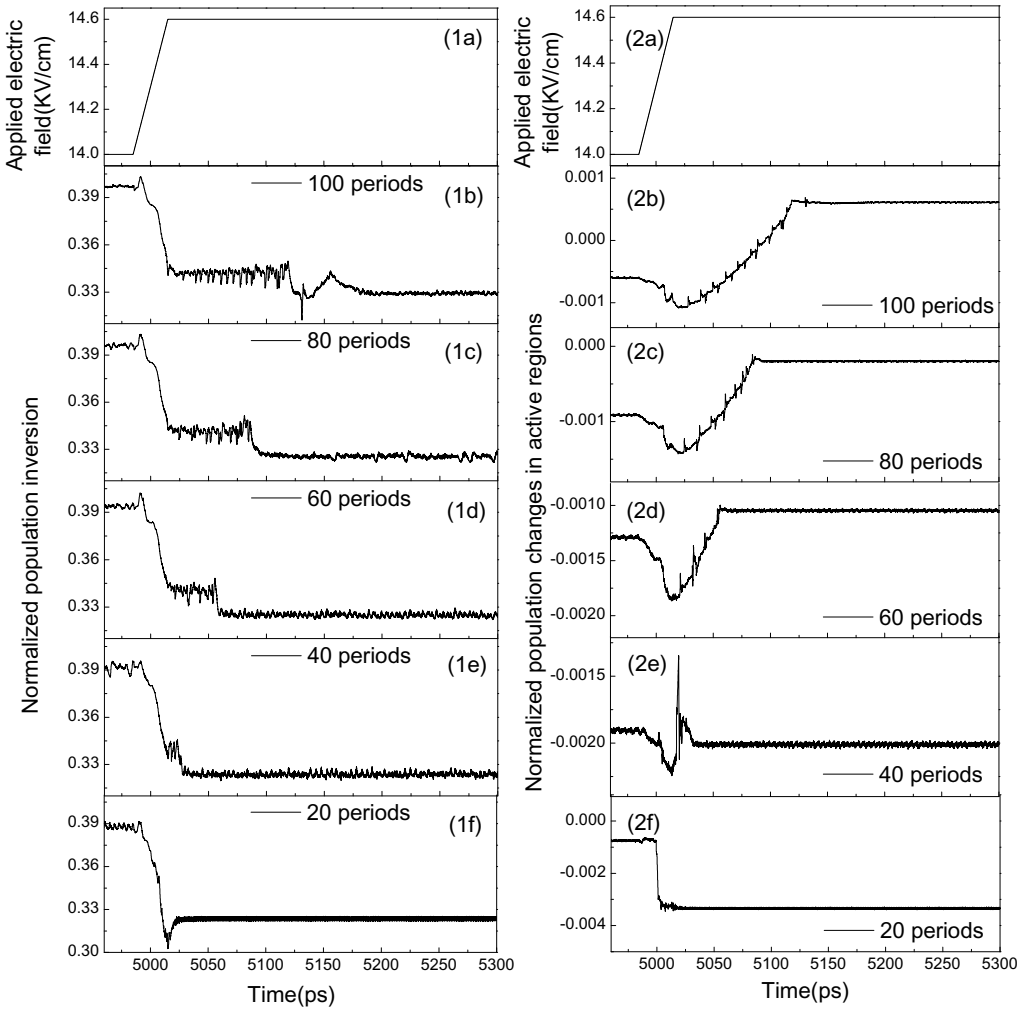

Figure 4. Detailed simulation results of normalized population inversions (1) and normalized population changes (2) with different period numbers 100 (1b), (2b), 80 (1c), (2c), 60 (1d), (2d), 40 (1e), (2e) and 20 (1f), (2f). Corresponding applied electric fields shown in (1a) and (2a).

understood by the established dynamic equilibrium of the electric potential in the cascade structure [8]. In figure 2(d), when the applied electric field changes, different equilibrium values of the population change are achieved. Compared with figure 2(c), we can find that the population changes in active regions have the similar properties, which means the existence of a long equilibrium establishment after both the falling and the rising edges. Population changes are less than $\pm 0.1\%$ and cannot severely affect the nonlinear distribution of the electric potential. Apparently, the equilibrium recovery processes shown in both figures 2(c) and (d) are achieved more slowly than the modulation process of the applied electric field.

In our previous work, the non-uniform electric potential was observed, but the nonlinear property was not distinguished clearly for the total cascade structure. In figure 3, we show the built-in electric potential and the electron density corresponding to the position in the total cascade structure. The applied electric field is $14.0\,\mathrm{kV\,cm^{-1}}$. Since the dynamic equilibrium is achieved, the results shown here are at a certain moment. Although non-uniformity is not

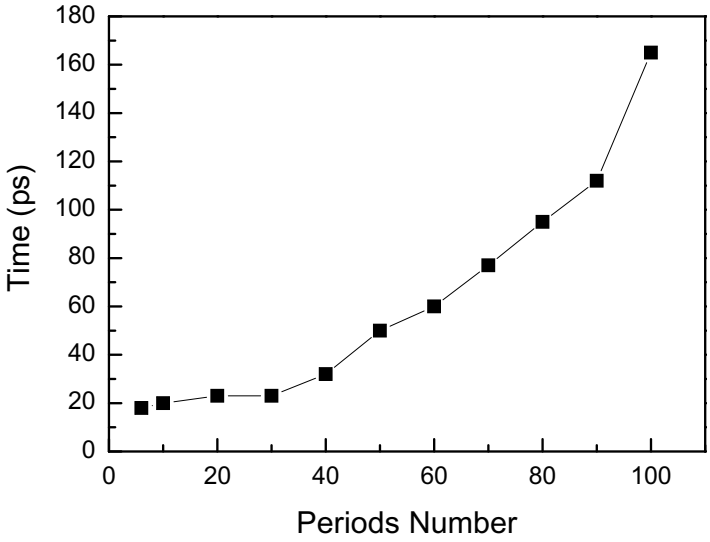

Figure 5. The equilibrium formation time as a function of the period number.

obvious enough, it is shown clearly in this figure. Electron accumulation and depletion are found beside the negative (the emitter contact) and the positive contact, respectively.

In figure 4, we focus on a small time scale and represent self-consistent results with different period numbers. The detailed differences can be observed clearly. We find non-equilibrium oscillations to appear in all cases of different period numbers and establishing the population equilibrium gets quicker as the period number gets smaller. In figure 4(1), in all cases, although equilibrium cannot be established quickly, the modulation depth of the population inversion is achieved deeply in a short time. In figure 4(2), first, we find that different equilibrium values of the population change are achieved with different period numbers and the same applied electric field. Second, compared with the deep achievement of population inversion modulation in a short time, time evolutions of the population change do not show the similar property. It means, population changes do not strongly affect the population inversions because they are extremely smaller than the total electron number in active regions.

We represent the equilibrium formation time as a function of the period number in figure 5. We can find that the time increases nonlinearly with the period number. It is the special finding by using the multi-period self-consistent equations. We give a qualitative explanation here. When the modulation arises, a long time is needed to establish the new electron distribution. There are two aspects that affect the equilibrium formation time. One is the length of the cascade structure. Some electrons are needed to transport out or into the cascade structure because the total electron number in active regions has been changed by the modulation. The other aspect is the difference between electron distributions before and after modulation. It is because, in the situation of the non-uniform electric potential, the electrons may not have to travel the total cascade structure to achieve equilibrium. If we neglect the built-in potential caused by the inhomogeneous electron distribution over the active regions, every period has the same electric potential, so the electrons injected from the emitter contact transport with the same scattering and tunneling mechanisms in different periods. In this hypothetical case, the equilibrium formation time should have a linear increasing relationship with the period number. From above discussions, we find that it is difficult to analyze the equilibrium formation time

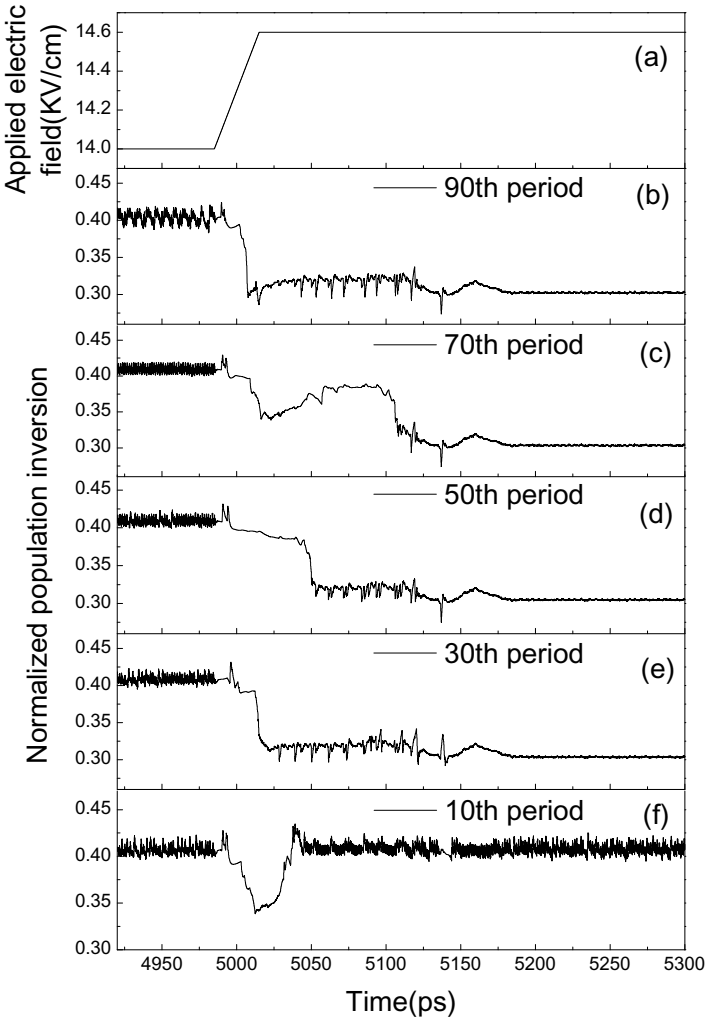

Figure 6. Normalized population inversion in 90th (b), 70th (c), 50th (d), 30th (e) and 10th (f) period. Corresponding applied electric fields shown in (a). The period number is 100.

quantitatively. In this work, the nonlinear distribution of the electric potential, which is caused by the nonlinear electron distribution in active regions, is presented and electrons transport in the multi-period with different scattering and resonant tunneling mechanisms in different periods. So, the relationship between the equilibrium formation time and the period number cannot simply be linear.

In order to have an in-depth view of the electron transport in the cascade structure, we set the period number at 100 and give time evolutions of the population inversion in different periods here. In figure 6, the detailed differences are obviously shown, corresponding to the same time scale in figure 4. The population inversion changes as quickly as the applied electric field changes in the 90th period in figure 6(b). But in figure 6(c), the result in the 70th period shows a strange trend of changing. A delayed response of the population inversion is found in the 50th period in figure 6(d). As for the result shown in figure 6(e), the quick response of the population dynamics in the 30th period is similar to the situation of the 90th period. In figure 6(f), it is interesting to find that population inversion in the 10th period has a fluctuation

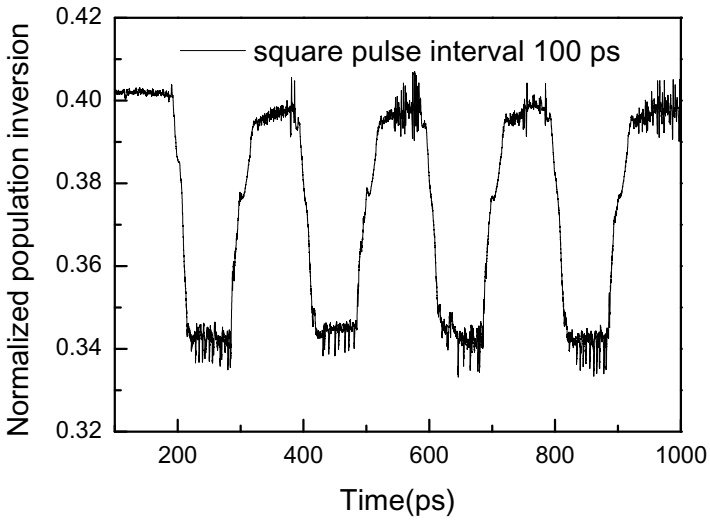

Figure 7. The modulated normalized population inversion with the modulation frequency 5 GHz. The period number is 100.

and then it almost recovers back to the same value. After the change of the applied electric field has been completed, the new equilibrium of the electric potential begins to be stabilized. So, the processes presented here can be recognized as the stabilizations of electric potentials. According to the above results, it seems that the electrical potentials in different periods have different responses to the changing applied electric field. So, the non-equilibrium oscillations in figure 2(c) can be directly explained here. The phenomena shown here stem from the non-uniform electron distribution. It brings different changes of the electron distributions before and after the modulation in different periods.

Fast modulations of QCLs by using RF synthesis have been realized up to gigahertz in the mid-infrared region. In the above calculation, the modulation frequency has been chosen lower than one gigahertz. As for the faster modulation above gigahertz, such as 5 GHz, the pulse width 100 ps is much smaller than the equilibrium formation time which is about 163 ps with the period number 100. So, the applied electric field changes again before the population equilibrium is achieved. Here, we represent the results of normalized population inversions with the modulation frequency 5 GHz in figure 7. The period number is set at 100. It is shown that the equilibrium states are not established well in the modulation. Compared with total equilibrium establishment provided in figure 1(c), we find that the achieved modulation depth is about 60% without signal distortion. The feasibility of AM in terahertz QCLs up to gigahertz is demonstrated here.

4. Conclusions

In conclusion, we study the ultrafast population dynamics in the electrically modulated three-well terahertz QCL by using the self-consistent Bloch–Poisson equations. After the applied electric field has been changed, non-equilibrium oscillations are found before the population inversion equilibrium recovers. From the results of population changes in the active regions, we also find that population equilibrium is not established quickly. The equilibrium formation time depends on two aspects: one is the length of the cascade structure and the other is the difference

between the electron distributions before and after the modulation. In this work, the non-uniform electron distribution in the active regions is presented, so the equilibrium-formation time increases nonlinearly with the period number. We also provide the changing population inversions in different periods. Different responses to the modulation of the applied electric field can be found apparently. Here, we can get the in-depth understanding of the physical mechanism that the electron transport obeys in the cascade structure. At last, we demonstrate that it is feasible to use terahertz QCLs with resonant-phonon design to realize AM in gigahertz frequency scale without signal distortion.

Acknowledgments

One of the authors (FW) thanks Z Chen for helpful discussions. This work was supported by the 863 Program of China (project number 2011AA010205), the National Natural Science Foundation of China (grant numbers 61131006, 61021064, 61176086 and 61204135), the Major National Development Project of Scientific Instrument and Equipment (grant number 2011YQ150021), the Important National Science and Technology Specific Projects (grant number 2011ZX02707), the major project (project number YYYJ-1123-1) and the International Collaboration and Innovation Program on High Mobility Materials Engineering of the Chinese Academy of Sciences, and the Shanghai Municipal Commission of Science and Technology (project number 10JC1417000 and 11ZR1444000).

References

[1] Köhler R, Tredicucci A, Beltram F, Beere H E, Linfield E H, Davies A G, Ritchie D A, Iotti R and Rossi F 2002 *Nature* **417** 156
[2] Williams B S 2007 *Nature Photon.* **1** 517
[3] Callebaut H and Hu Q 2005 *J. Appl. Phys.* **98** 104505
[4] Han Y J, Feng W and Cao J C 2012 *J. Appl. Phys.* **111** 113111
[5] Kumar S and Hu Q 2009 *Phys. Rev.* B **80** 245316
[6] Dupont E, Fathololoumi S and Liu H C 2010 *Phys. Rev.* B **81** 205311
[7] Wang F, Guo X G and Cao J C 2010 *J. Appl. Phys.* **108** 083714
[8] Wang F, Guo X G, Li H and Cao J C 2012 *Appl. Phys. Lett.* **100** 102102
[9] Barbieri S, Maineult W, Dhillon S S, Sirtori C, Alton J, Breuil N, Beere H E and Ritchie D A 2007 *Appl. Phys. Lett.* **91** 143510
[10] Gellie P *et al* 2010 *Opt. Express* **20** 20799
[11] Capasso F *et al* 2002 *IEEE J. Quantum Electron.* **38** 511
[12] Chen Z, Gu L, Tan Z Y, Wang C and Cao J C *IEEE Electron Letter* (submitted)
[13] Barbieri S, Ravaro M, Gellie P, Santarelli G, Manquest C, Sirtori C, Khanna S P, Linfield E H and Davies A G 2011 *Nature Photon.* **5** 306
[14] Freeman J R, Maysonnave J, Jukam N, Cavalié P, Maussang K, Beere H E, Ritchie D A, Mangeney J, Dhillon S S and Tignon J 2012 *Appl. Phys. Lett.* **101** 181115
[15] Luo H, Laframboise S R, Wasilewski Z R, Aers G C, Liu H C and Cao J C 2007 *Appl. Phys. Lett.* **90** 041112
[16] Kumar S, Hu Q and Reno J L 2009 *Appl. Phys. Lett.* **94** 131105
[17] Fathololoumi S, Dupont E, Chan C W I, Wasilewski Z R, Laframboise S R, Ban D, Mátyás A, Jirauschek C, Hu Q and Liu H C 2012 *Opt. Express* **20** 3866
[18] Pan J L and Fonstad C G Jr 1999 *IEEE J. Quantum Electron.* **35** 1673
[19] Rosencher E, Luc F, Bois Ph and Delaitre S 1992 *Appl. Phys. Lett.* **61** 468
[20] Ferry D K and Goodnick S M 1999 *Transport in Nanostructures* (Cambridge: Cambridge University Press)